# Adaptive Optics Imaging of Healthy and Abnormal Regions of Retinal Nerve Fiber Bundles of Patients With Glaucoma

Monica F. Chen,[1] Toco Y. P. Chui,[2,3] Paula Alhadeff,[2] Richard B. Rosen,[2,3] Robert Ritch,[2] Alfredo Dubra,[4] and Donald C. Hood[1,5]

[1]Department of Psychology, Columbia University, New York, New York, United States
[2]New York Eye and Ear Infirmary of Mount Sinai, New York, New York, United States
[3]Department of Ophthalmology, Icahn School of Medicine at Mount Sinai, New York, New York, United States
[4]Medical College of Wisconsin, Milwaukee, Wisconsin, United States
[5]Department of Ophthalmology, Columbia University, New York, New York, United States

Correspondence: Donald C. Hood, Department of Psychology, 406 Schermerhorn Hall, 1190 Amsterdam Avenue, MC 5501, Columbia University, New York, NY 10027, USA; dch3@columbia.edu.

Submitted: October 26, 2014
Accepted: December 21, 2014

Citation: Chen MF, Chui TYP, Alhadeff P, et al. Adaptive optics imaging of healthy and abnormal regions of retinal nerve fiber bundles of patients with glaucoma. *Invest Ophthalmol Vis Sci*. 2015;56:674–681. DOI:10.1167/iovs.14-15936

**Purpose.** To better understand the nature of glaucomatous damage of the macula, especially the structural changes seen between relatively healthy and clearly abnormal (AB) retinal regions, using an adaptive optics scanning light ophthalmoscope (AO-SLO).

**Methods.** Adaptive optics SLO images and optical coherence tomography (OCT) vertical line scans were obtained on one eye of seven glaucoma patients, with relatively deep local arcuate defects on the 10-2 visual field test in one (six eyes) or both hemifields (one eye). Based on the OCT images, the retinal nerve fiber (RNF) layer was divided into two regions: (1) within normal limits (WNL), relative RNF layer thickness within mean control values ±2 SD; and (2) AB, relative thickness less than −2 SD value.

**Results.** As seen on AO-SLO, the pattern of AB RNF bundles near the border of the WNL and AB regions differed across eyes. There were normal-appearing bundles in the WNL region of all eyes and AB-appearing bundles near the border with the AB region. This region with AB bundles ranged in extent from a few bundles to the entire AB region in the case of one eye. All other eyes had a large AB region without bundles. However, in two of these eyes, a few bundles were seen within this region of otherwise missing bundles.

**Conclusions.** The AO-SLO images revealed details of glaucomatous damage that are difficult, if not impossible, to see with current OCT technology. Adaptive optics SLO may prove useful in following progression in clinical trials, or in disease management, if AO-SLO becomes widely available and easy to use.

Keywords: glaucoma, adaptive optics, optical coherence tomography, retinal nerve fiber layer

Everyday visual functions depend on the integrity of the fovea and the surrounding central macular region, defined here as the central ±8°. Although it has long been recognized that early glaucomatous damage can affect the macula, until recently such damage has been largely ignored, as evidenced by the widespread use of the 24-2 visual field (VF) test pattern, which poorly samples macular damage.[1–6] Recently, there has been renewed interest in studying macular damage now that in vivo measures of the retinal nerve fiber (RNF) layer and retinal ganglion cell (RGC) layer thickness can be made with frequency-domain optical coherence tomography (fdOCT). Combined VF and fdOCT data clearly indicate that glaucomatous damage to the macula is common, can occur early in the disease, involves both deep local and shallow widespread loss of VF sensitivity, and is accompanied by a range of RNF and RGC layer thinning.[7–9] Here, we focus on glaucoma patients with deep, local VF damage and extensive RNF layer thinning in the macula region.

To identify RNF layer loss, a number of imaging methods have been used, including fundus photography,[10–13] scanning laser polarimetry,[14–19] scanning laser ophthalmoscopy,[20–22] and OCT.[23–30] However, none of these modalities have the necessary lateral resolution to allow the study of RNF bundles, primarily because of aberrations in ocular optics.

Adaptive optics instruments compensate for the aberrations of the eye.[31] Although early work largely studied the photoreceptors,[32–36] recent advances to the adaptive optics scanning light ophthalmoscope (AO-SLO) have allowed for unprecedented in vivo visualization of retinal features, including retinal pigment epithelium cells, microvasculature, vascular flow, and the lamina cribrosa.[37–47] Further, it has been recently shown that the RNF bundles can be imaged in controls and patients with glaucoma.[48–52]

The purpose of this study was to use AO-SLO data to better understand the nature of local damage of the macula in glaucoma patients. We were particularly interested in the AO-SLO appearance of the RNF bundles in and around the transition from the relatively healthy to clearly abnormal (AB) regions, as it is a likely site of disease progression.

## Methods

### Subjects

Subjects with deep, local arcuate defects (at least five test points ≤ −15 dB) on the 10-2 VF total deviation plot (Humphrey VF Analyzer; Carl Zeiss Meditec, Inc., Dublin, CA,

USA) were recruited from New York Eye and Ear Infirmary of Mount Sinai. Inclusion criteria included refraction within ±4.0 diopters, pupil dilation of at least 6 mm, clear media, and good central fixation with a best-corrected visual acuity better than 20/40. Patients with unreliable VF results and media opacities were excluded. All patients had fdOCT scans, 10-2 VFs, and AO-SLO imaging within 1 year.

One eye of 10 open-angle glaucoma patients (60.7 ± 7.9 years) was prospectively tested, but three eyes had to be excluded. In one eye, the presence of an epiretinal membrane made it difficult to visualize the RNF bundles. In a second eye, the AO images were of insufficient quality for the analysis. In the third eye, the defect was too close to the fovea center, and too extensive, to see a region of RNF thickness within normal limits (WNL). Thus, we studied eight hemi-retinas in seven eyes, although the three eyes removed, to the extent we could analyze the images, showed the same pattern of results.

The study was approved by the Columbia University and New York Eye and Ear Infirmary of Mount Sinai Institutional Review Boards and adheres to the tenets set forth in the Declaration of Helsinki and the Health Insurance Portability and Accountability Act. Written informed consent was obtained from all subjects.

## Swedish Interactive Threshold Algorithm (SITA)-Standard Protocol

The 10-2 VFs were obtained with the SITA-standard automated perimetry and all met reliability criteria (fixation losses ≤ 20%, false positives ≤ 5%, and false negatives ≤ 10%). Both hemi-retinas of the 10-2 VF were AB in one of the seven eyes, and the other eyes had defects in the lower retina/upper VF.

## Frequency-Domain OCT

All patients had vertical line scans of the macula (6 mm, 1024 A-scans with at least 16 overlapping averages [3D-OCT 1000/2000; Topcon Corp., Paramus, NJ, USA]). The RNF layer of the OCT scans was segmented (Fig. 1A) using a computer-assisted manual segmentation technique.[53,54] The green and red lines in Figure 1A show the borders of inner limiting membrane/vitreous (green) and RNF/RGC layer (red) on a macular vertical line scan. The distance between these lines is the RNF layer thickness.

For each eye, RNF layer thickness was plotted versus distance from the fovea center as shown by the magenta curve in Figure 1B for the scan in Figure 1A. The black curve in Figure 1B is the mean thickness from 54 healthy eyes[7] (age 53.2 ± 8.1 years) and the gray curves are the ±2 SD values. The region below the 95% confidence interval (in the pink region) was considered AB. The region occluded by the gray rectangle corresponds to the central foveal region where the RNF layer was very thin, as well as variable across individuals.

The RNF layer was divided into two regions: (1) WNL, portion of the curve falling above the lower gray curve (above the pink region) in Figure 1B; and (2) AB, portion of the curve falling below the gray curve (–2 SD) (in the pink region) in Figure 1B.

## Adaptive Optics SLO Imaging

Confocal AO-SLO imaging using 790-nm light was performed using a previously described custom instrument.[55] The confocal pinhole size was approximately three times the Airy disk diameter as measured at the detector plane. Pupils were dilated with one drop of 2.5% phenylephrine hydrochloride ophthalmic solution (Bausch & Lomb, Inc., Tampa, FL, USA) and 1% tropicamide ophthalmic solution (Akorn, Inc., Lake Forest, IL, USA). Subjects were positioned using a dental impression on a bite bar (Splash! Putty; DenMat Holdings, LLC, Lompoc, CA, USA) and were instructed to gaze at an internal fixation target. The fixation target was moved along the vertical meridian such that the desired region of interest was in view.

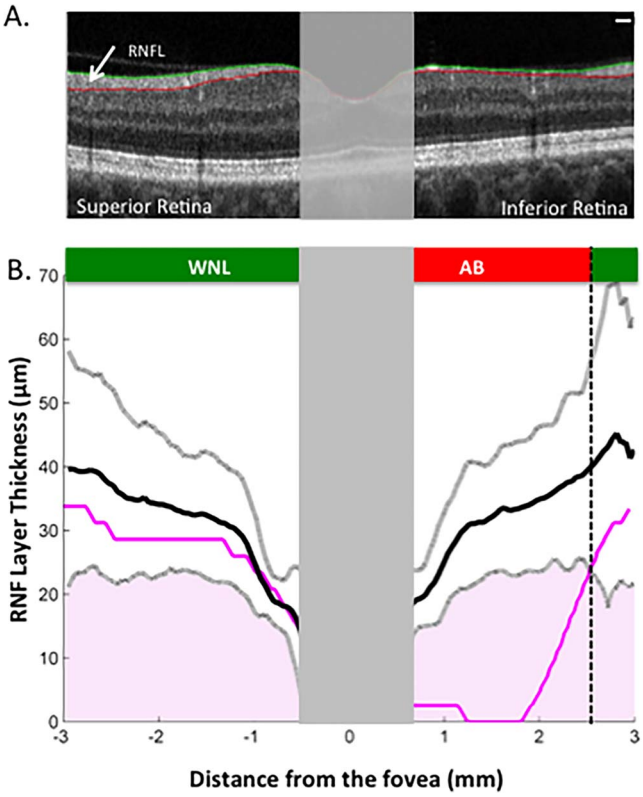


**Figure 1.** Measurements from fdOCT for patient 1. (**A**) A vertical fdOCT line scan through the fovea of a patient with glaucoma with the RNF layer borders segmented (*green* and *red lines*). (**B**) Retinal nerve fiber layer thickness along the line scan in (**A**) (*magenta*), along with the mean (*black*) and ±2 SD (*gray*) of scans from 54 healthy controls. The foveal region is occluded because the RNF layer thickness is thin, as well as variable across individuals. The RNF layer was divided into two regions: (1) WNL, RNF layer thickness above the –2 SD boundary (above the *pink region*), and (2) AB, RNF layer thickness below the –2 SD (in the *pink region*). *Scale bar*: 200 µm.

Retinal nerve fiber bundles were imaged along a 20° vertical line centered at the fovea. After the features were located and in focus, confocal reflectance sequences of 150 frames were captured using a 1° square field of view. The RNF layer focus was determined by maximizing image sharpness (qualitatively) of the innermost RNF layer boundary. The overall imaging time was approximately 40 minutes, including short breaks as needed. Frames in each sequence were registered and averaged to generate images with high signal-to-noise ratio.[56] The resulting images were manually montaged and then coregistered with high-quality fundus photographs using Photoshop CS6 (Adobe Systems, Inc., San Jose, CA, USA). The OCT images were registered to the same fundus photographs for comparison with the AO-SLO images.

To calculate the AO-SLO image scale in microns per pixel, axial length measurements were obtained using an IOL Master (Carl Zeiss Meditec, Inc.). The calculations of individual retinal magnification factors were based on the Emsley schematic eye model.[57] These magnification factors were then applied to the AO-SLO images.

Investigative Ophthalmology & Visual Science

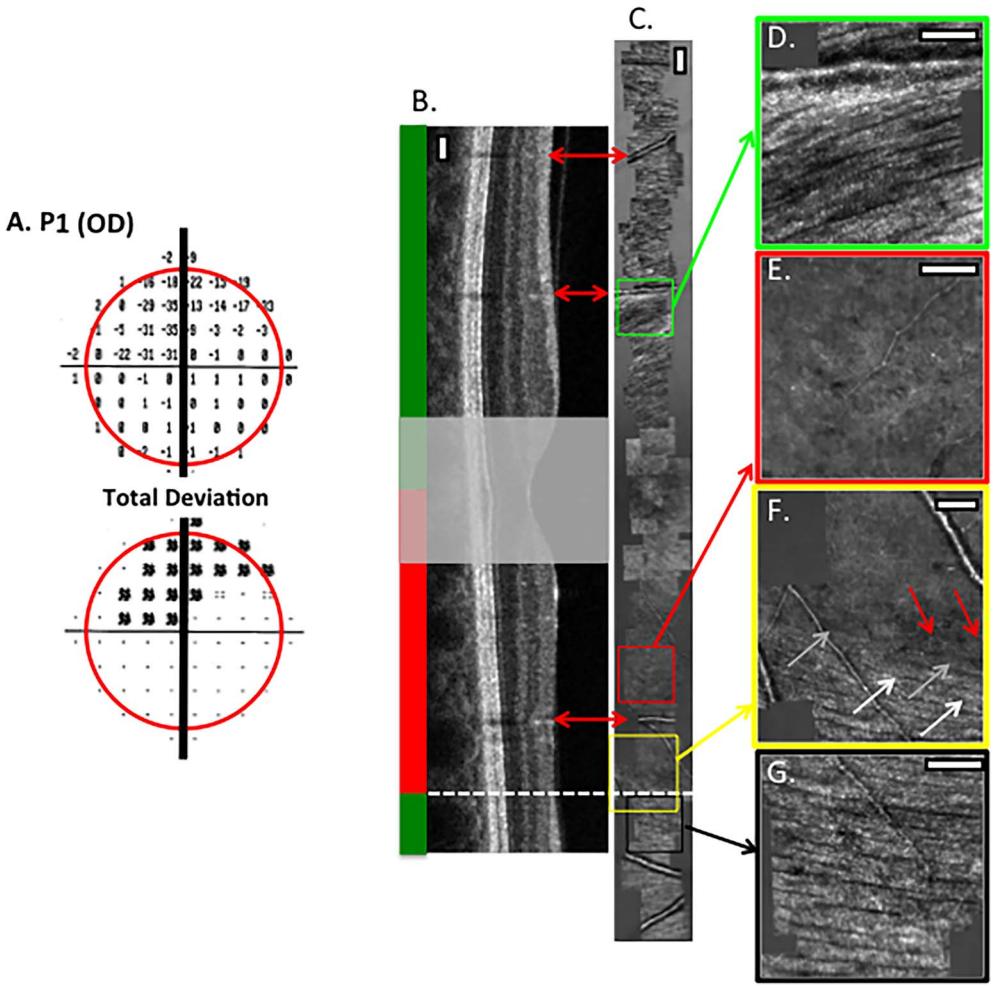


FIGURE 2. (**A**) The 10-2 total deviation plots for patient 1. (**B**) The vertical line scan from Figure 1A. (**C**) The AO-SLO images for the same region aligned with the OCT scan using the blood vessels as indicated by the *red arrows*. (**D–G**) Enlarged portions of the AO-SLO images. *Scale bars*: 200 μm (**B**, **C**); 100 μm (**D–G**).

## RESULTS

Eight hemi-retinas (seven eyes) had relatively deep, arcuate defects in the central ±10° as shown for P1 and P2 in Figures 2A and 3A, respectively; P2 is the eye with both hemifields AB on VF (Fig. 3A). The vertical OCT scan (B) and AO-SLO images (C, D) for these patients are also shown in Figures 2 and 3. To compare these images, they were aligned using blood vessels as indicated by the red arrows between B and C. The green and red bars on the left of B show the WNL (green) and AB (red) regions as defined for this patient based on the RNF layer thickness analysis in Figure 1C. The border between the WNL and AB regions is shown as the white dashed line in B and C. In five hemi-retinas (five eyes), the white dashed line marked the trailing edge (farthest from the fovea) of the defect as in Figure 2, as the defect was too close to the foveal center to visualize the RNF bundles of the leading edge. In three hemi-retinas (three eyes), the leading edge was seen as shown in Figure 3. The results described below were the same for leading and trailing edges.

The AO-SLO images clearly differed in the OCT-defined WNL and AB regions of Figure 2. In the AB region, RNF bundles were not seen. For example, compare the AB region in Figure 2E to the WNL region in Figure 2D, which is equidistant from the foveal center. In the WNL region adjacent to the AB region, the RNF bundles (Fig. 2G) also appear similar to those in the healthy region (Fig. 2D). Finally, the transition region between the relatively normal RNF bundles and regions without bundles is very narrow. Figure 2F shows a blow up of this region with arrows pointing to areas of relatively normal (white) and missing (red) RNF bundles. The gray arrows point to regions with abnormally appearing RNF bundles of lower contrast.

To describe the results of the other seven hemi-retinas (six eyes), we can use the results in Figure 2 as an archetypical pattern. In particular, we define this archetypical pattern as clearly apparent bundles within the WNL region, absent or very difficult to discern bundles in the AB region, and a narrow region of bundles of poor contrast at the border between the WNL and AB regions.

### Adaptive Optics SLO Images Within OCT-Defined WNL Region

Consistent with the archetypical pattern, seven of the eight AB hemi-retinas had clear bundles in the WNL regions (see Figs. 2D, 2G, 3E, white arrow); in one eye, the WNL was too small and too close to fovea to assess. In all hemi-retinas, AO-SLO images showed high-contrast RNF bundles, with the packing density of the bundles dependent on eccentricity, as previously reported.[49,50] However, in four of the eight AB hemi-retinas (four eyes), bundles with markedly reduced contrast were also seen in the WNL region. This is not surprising; although these

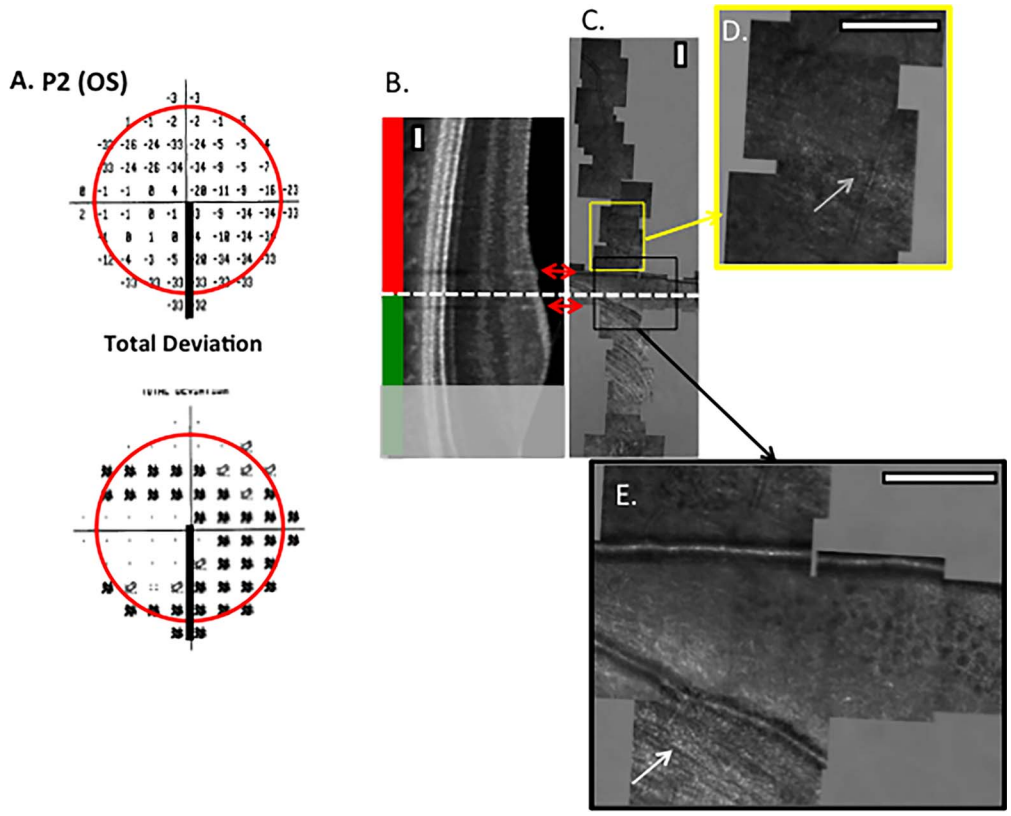


FIGURE 3. (**A**) The 10-2 VF total deviation plots for patient 2. (**B**) The vertical line scan for patient 2. (**C**) The AO-SLO images for the same region aligned with the OCT scan using the blood vessels as indicated by the *red arrows*. *Scale bars*: 200 μm.

regions had RNF layer thickness WNL on OCT, they were often thinner than average compared with controls. On the other hand, regions without RNF bundles were not seen in the WNL regions in any eyes.

### Adaptive Optics SLO Images at the Border of OCT-Defined AB and WNL Regions

Similar to the archetypical pattern, four AB hemi-retinas (three eyes) had relatively abrupt border between the WNL and AB regions containing a few bundles of lower contrast, as shown in Figures 2F and 3E. However, in four hemi-retinas (four eyes), this region was not abrupt; P5 is an extreme example, as bundles could be discerned throughout the AB region (Fig. 4A). Although a clear transition was seen in the other three eyes, the region with AB bundles varied in width from 0.75 to 3°.

### Adaptive Optics SLO Images Within AB Region on OCT

Like the archetypical pattern, the AB regions had areas without RNF bundles in all but one hemi-retina (P5, Fig. 4A). In six of the eyes, the AB region contained dark, circular structures 5 to 25 μm in diameter, as seen in Figure 4B for two of the eyes. Although the size of these structures is consistent with RGCs, displaced amacrine cells, and/or portions of Müller cells, we cannot be sure of their origin.

In addition to P5 (Fig. 4A), two hemi-retinas (two eyes) differed from the archetypical pattern in having bundles well within the AB region, not simply at the border with the WNL. Interestingly, in these two hemi-retinas, a small area of bundles with reduced contrast was sandwiched between regions without bundles; P2 had one of these regions (Fig. 3D, gray arrow). The other region, shown for P4 in Figure 4C, is easier to discern. Notice there are clear bundles within the gray rectangle with regions without bundles (red arrows) both above and below.

## DISCUSSION

Using AO-SLO, we examined the RNF bundles in relatively healthy and clearly AB retinal regions in the vicinity of local arcuate defects of the macula. Below we summarize the appearance of these regions and then discuss the implications for following progression.

### The Appearance In and Around Regions of Arcuate Damage

To organize the results, we defined an archetypical pattern. The archetype had a WNL region with normal-appearing bundles, an AB region without bundles, and a relatively sharp border between them with only a few AB bundles with reduced contrast. Only two hemi-retinas (two eyes) approximated this pattern. Other hemi-retinas differed from the archetype. First, four hemi-retinas (four eyes) contained a relatively wide region of AB-appearing bundles of uneven and lower contrast on one or both sides of the border between the WNL and AB regions. One hemi-retina appeared to have bundles throughout the AB region, although they were of lower contrast and barely visible in places. Second, two hemi-

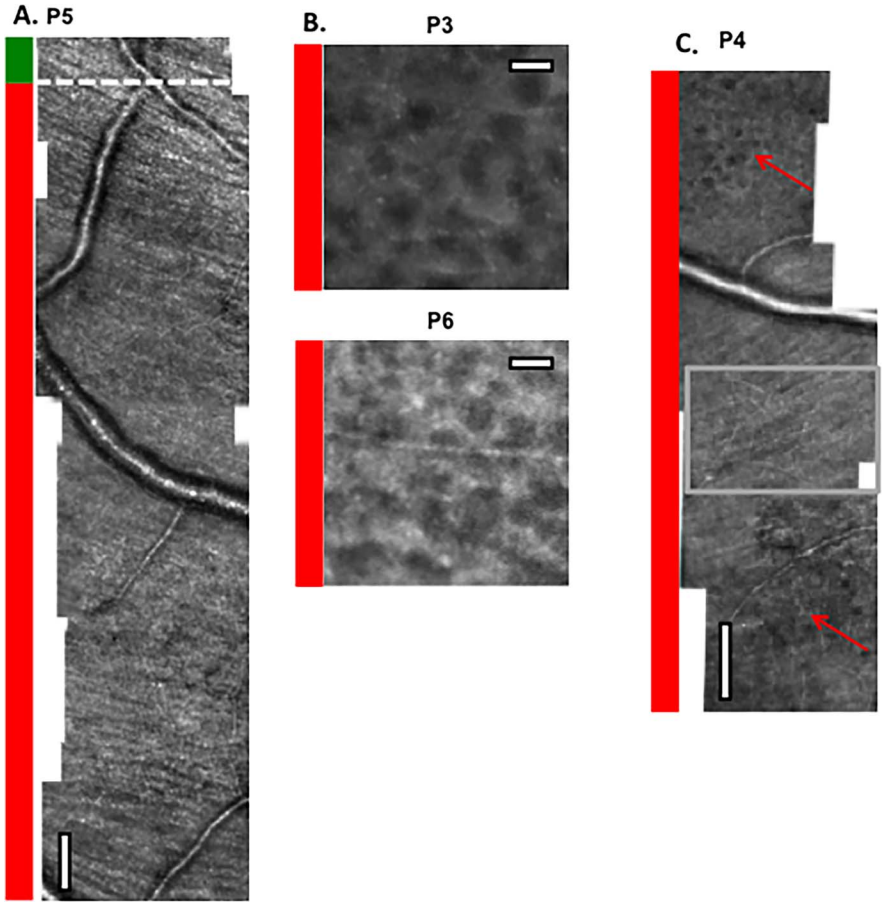


**Figure 4.** Examples of AO-SLO images within OCT-defined AB regions. (**A**) Retinal nerve fiber bundles seen throughout the AB region. (**B**) The AB regions without RNF bundles and with circular structures. (**C**) Retinal nerve fiber bundles (*gray rectangle*) sandwiched between regions without RNF bundles (*red arrows*). *Scale bars*: 100 μm (**A**, **C**); 25 μm (**B**).

retinas (two eyes) had clear bundles well within the AB region; these were sandwiched between regions without bundles.

These results are easy to reconcile with what we know of glaucomatous damage, which is assumed to occur at the disc. Assume, for example, that the damage at the disc was local and complete, destroying all local axons in a region, but preserving the neighbors. This local and complete damage should result in the archetypical pattern of damage. Although the archetypical pattern was seen in two eyes, the others exhibited other patterns of damage. Thus, the AO-SLO results suggest that the RNF damage at the disc is not homogeneous. Uneven damage can leave islands of RNF bundles and incompletely damaged regions of AB-appearing bundles.

Although the pattern of results we observe is not surprising, it is easier to see these patterns with AO-SLO due to the superior spatial resolution compared with that of perimetry or OCT. Figure 5 illustrates the difference in spatial detail possible between the AO-SLO used here and a commercial fdOCT scan. This image is from the same general region shown in Figure 4C, but it covers a larger area with a lower magnification. The gray arrow in Figure 5 points to the same rectangular region with preserved bundles seen in Figure 4C. Although it is possible that this region corresponds to the region with the white arrow with the question mark on the fdOCT in Figure 5A, it is hard to be certain. In any case, the details seen on AO-SLO are certainly lost. Another example can be seen in Figure 5B, where there appears to be an AB region of one or two bundles in a region of normal-appearing bundles.

## Possible Implications for Following Progression

Detecting and following the progression of glaucomatous damage is a challenge for the clinician. Although AO-SLO is not ready for routine clinical use (see limitations below), it may provide a way to better understand progression and even to detect it in clinical trials. The edge of the archetypical defect, the isolated region of preserved bundles, and the AB-appearing bundles within damaged regions are potential locations for detecting progression. It is certainly possible that an examination of these regions with AO-SLO will detect progression sooner than perimetry or clinical OCT scans, given the difference in spatial resolution discussed above. Of course, this assumes that these regions are likely locations for progression. Su et al.[58] simulated a group of eyes with extended follow-up with a cross-sectional analysis of the 10-2 VFs from 80 eyes with local macular defects similar to those in the present study. According to their analysis, these defects widened and deepened over time. Previous OCT data from two of the patients in the current study support this conclusion. In particular, P1 had a circumpapillary circle scan at the time of the AO-SLO imaging, as well as one approximately 28 months earlier. The width of the RNF layer defect increased between the two tests. Similarly, the width of both the superior and inferior RNF defects seen for P2 on circumpapillary circle scans increased in width over a 35-month period. Whether local regions of preserved bundles seen on AO-SLO also will change with time remains to be tested.

Investigative Ophthalmology & Visual Science

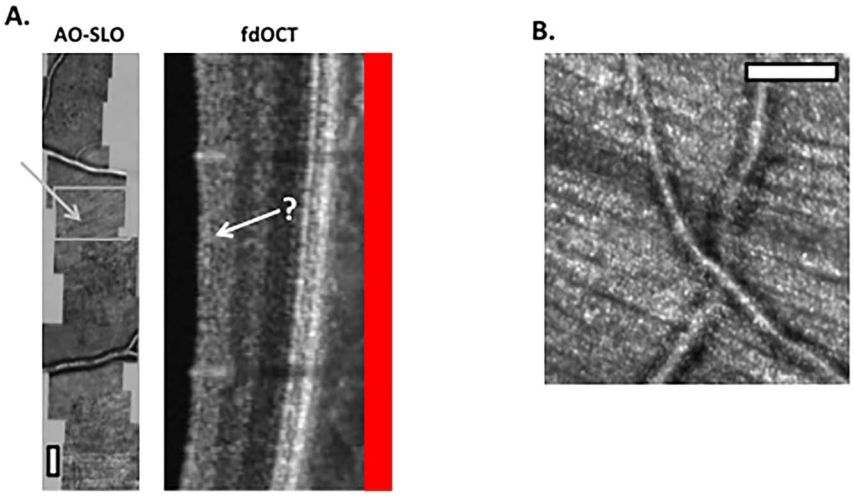


FIGURE 5. **(A)** Adaptive optics SLO images and an fdOCT scan of the same region of the retina of patient 4, the patient with the preserved RNF bundles shown in Figure 4C. The *gray rectangle* corresponds to the *gray rectangle* in Figure 4C. These preserved RNF bundles are difficult to see on the fdOCT scan (*white arrow*). **(B)** An AB region of one or two bundles within a region of normal-appearing bundles. *Scale bars*: 100 μm.

## Limitations and Caveats

Although it is relatively easy to distinguish regions without bundles from those with bundles, we do not have a good quantitative measure of the spectrum from normal, healthy bundles to those that are just barely perceptible. For our purposes here, we used "normal-appearing," and "clearly reduced in contrast." Although contrast is a natural possible measure, there is a range of contrasts seen in healthy controls. Perhaps in the future it will be possible to develop a contrast that is normalized for eccentricity and for individual scan quality. Alternatively, with appropriately matched healthy controls, perhaps RNF bundle width may prove useful.[50]

In terms of caveats, AO-SLO is not ready for routine clinical use. First, it is difficult to get acceptable images on patients with cataracts, dry eyes, small pupils, high refractive error, or, as we have learned, with epiretinal membranes in the region of interest. Second, the images obtained here took approximately 40 minutes to obtain. Finally, data analysis is time consuming, as the image registration software and the montaging require extensive user input. On the other hand, as stated above, AO-SLO should be a viable technique in clinical trials in which a measure of progression (or improvement) is needed. For this purpose, restricting imaging to local regions of interest could substantially shorten the time for both imaging and analysis.

## Summary and Clinical Implications

With AO-SLO, the details near the borders between OCT-measured RNF layer thickness within and outside normal limits can be visualized. These are possible regions of progression of glaucomatous damage and one can see details in these regions that are difficult or impossible to see using OCT scans, or to measure using perimetry. Thus, AO-SLO may have a role in clinical trials needing a measure of progression.

### *Acknowledgments*

The authors thank Ali Raza for his assistance at various stages of this project; Benjamin Epstein, Dongwon Lee, and Jason Nunez for their assistance in the preparation of this manuscript; and Alexander Gan, Alexander Pinhas, Moataz Razeen, Nishit Shah, Michael Dubow, and Daiyan Xin for their assistance imaging the patients.

Supported by National Institutes of Health Grants EY-02115 and EY-14375, and grants from Research to Prevent Blindness (Career Award [AD] and Departmental Award), Glaucoma Research Foundation, the Marrus Family Foundation, Bendheim-Lowenstein Family Foundation, Wise Family Foundation, R.D. and Linda Peters Foundation, Edith C. Blum Foundation, and Chairman's Research Fund of the New York Eye and Ear Infirmary.

Disclosure: **M.F. Chen**, None; **T.Y.P. Chui**, None; **P. Alhadeff**, None; **R.B. Rosen**, None; **R. Ritch**, None; **A. Dubra**, Canon USA (F), P; **D.C. Hood**, Topcon, Inc. (F, C)

### *References*

1. Aulhorn E, Harms M. Early visual field defects in glaucoma. In: Leydhecker W, ed. *Glaucoma, Tutzing Symposium*. Basel, Switzerland: Karger; 1967:151–156.
2. Drance SM. The early field defects in glaucoma. *Invest Ophthalmol*. 1969;8:84–91.
3. Aulhorn E, Karmeyer H. Frequency distribution in early glaucomatous visual field defects. *Doc Ophthalmol Proc Ser*. 1977;14:75–83.
4. Nicholas SP, Werner EB. Location of early glaucomatous visual field defects. *Can J Ophthalmol*. 1980;15:131–133.
5. Anctil JL, Anderson DR. Early foveal involvement and generalized depression of the visual field in glaucoma. *Arch Ophthalmol*. 1984;102:363–370.
6. Heijl A, Lundqvist L. The frequency distribution of earliest glaucomatous visual field defects documented by automatic perimetry. *Acta Ophthalmol (Copenh)*. 1984;62:658–664.
7. Hood DC, Raza AS, de Moraes CG, Johnson CA, Liebmann JM, Ritch R. The nature of macular damage in glaucoma as revealed by averaging optical coherence tomography data. *Transl Vis Sci Technol*. 2012;1:1–15.
8. Hood DC, Raza AS, de Moraes CG, Liebmann JM, Ritch R. Glaucomatous damage of the macula. *Prog Retin Eye Res*. 2013;32:1–21.
9. Hood DC, Slobodnick A, Raza AS, de Moraes CG, Teng CC, Ritch R. Early glaucoma involves both deep local, and shallow widespread, retinal nerve fiber damage of the macular region. *Invest Ophthalmol Vis Sci*. 2014;55:632–649.
10. Hoyt WF, Frisen L, Newman NM. Fundoscopy of nerve fiber layer defects in glaucoma. *Invest Ophthalmol*. 1973;12:814–829.

11. Miller NR, George TW. Monochromatic (red-free) photography and ophthalmoscopy of the peripapillary retinal nerve fiber layer. *Invest Ophthalmol Vis Sci*. 1978;17:1121–1124.
12. Quigley HA, Reacher M, Katz J, Strahlman E, Gilbert D, Scott R. Quantitative grading of nerve fiber layer photographs. *Ophthalmology*. 1993;100:1800–1807.
13. Muramatsu C, Nakagawa T, Sawada A, et al. Automated segmentation of optic disc region on retinal fundus photographs: comparison of countour modeling and pixel classification methods. *Comput Methods Programs Biomed*. 2011; 101:23–32.
14. Greenfield DS, Knighton RW, Huang XR. Effect of corneal polarization axis on assessment of retinal nerve fiber layer thickness by scanning laser polarimetry. *Am J Ophthalmol*. 2000;129:715–722.
15. Choplin NT, Zhou Q, Knighton RW. Effect of individualized compensation for anterior segment birefringence on retinal nerve fiber layer assessments as determined by scanning laser polarimetry. *Ophthalmology*. 2003;100:719–725.
16. Sehi M, Ume S, Greenfield DS. Scanning laser polarimetry with enhanced corneal compensation and optical coherence tomography in normal and glaucomatous eyes. *Invest Ophthalmol Vis Sci*. 2007;48:2099–2104.
17. Monteiro MLR, Moura FC. Comparison of the GDx VCC scanning laser polarimeter and the stratus optical coherence tomography in the detection of band atrophy of the optic nerve. *Eye*. 2008;22:641–648.
18. Horn FK, Mardin CY, Laemmer R, et al. Correlation between local glaucomatous visual field defects and loss of nerve fiber layer thickness measured with polarimetry and spectral domain OCT. *Invest Ophthalmol Vis Sci*. 2009;50:1971–1977.
19. Medeiros FA, Alencar LM, Zangwill LM, et al. Detection of progressive retinal nerve fiber layer loss in glaucoma using scanning laser polarimetry with variable corneal compensation. *Invest Ophthalmol Vis Sci*. 2009;50:1675–1681.
20. Caprioli J, Park HJ, Ugurlu S, Hoffman D. Slope of the peripapillary nerve fiber layer surface in glaucoma. *Invest Ophthalmol Vis Sci*. 1998;39:2321–2328.
21. Bowd C, Zangwill LM, Medeiros FA, et al. Structure–function relationships using confocal scanning laser ophthalmoscopy, optical coherence tomography, and scanning laser polarimetry. *Invest Ophthalmol Vis Sci*. 2006;47:2889–2895.
22. Budenz DL, Chang RT, Huang X, Knighton RW, Tielsch JM. Reproducibility of retinal nerve fiber thickness measurements using the Stratus OCT in normal and glaucomatous eyes. *Invest Ophthalmol Vis Sci*. 2005;46:2440–2443.
23. Kim TW, Park UC, Park KH, Kim DM. Ability of stratus OCT to identify localized retinal nerve fiber layer defects in patients with normal standard automated perimetry results. *Invest Ophthalmol Vis Sci*. 2007;48:1635–1641.
24. Harwerth RS, Wheat JL, Rangaswamy NV. Age-related losses of retinal ganglion cells and axons. *Invest Ophthalmol Vis Sci*. 2008;49:4437–4443.
25. Lu ATH, Wang MW, Verma R, et al. Combining nerve fiber layer parameters to optimize glaucoma diagnosis with optical coherence tomography. *Ophthalmology*. 2008;115:1352–1357.
26. Costa-Cunha LV, Cunha LP, Malta RF, Monteiro ML. Comparison of Fourier-domain and time-domain optical coherence tomography in the detection of band atrophy of the optic nerve. *Am J Ophthalmol*. 2009;147:56–63.
27. Horn FK, Mardin CY, Laemmer R, et al. Correlation between local glaucomatous visual field defects and loss of nerve fiber layer thickness measured with polarimetry and spectral domain OCT. *Invest Ophthalmol Vis Sci*. 2009;50:1971–1977.
28. Seong M, Sung KR, Choi EH, et al. Macular and peripapillary retinal nerve fiber layer measurements by spectral domain optical coherence tomography in normal-tension glaucoma. *Invest Ophthalmol Vis Sci*. 2010;51:1446–1452.
29. Sakamoto A, Hangai M, Nukada M, et al. Three-dimensional imaging of macular retinal nerve fiber layer in glaucoma using spectral-domain optical coherence tomography. *Invest Ophthalmol Vis Sci*. 2010;51:5062–5070.
30. Wang M, Hood DC, Cho JS, et al. Measurement of local retinal ganglion cell layer thickness in patients with glaucoma using frequency-domain optical coherence tomography. *Arch Ophthalmol*. 2009;127:875–881.
31. Rossi EA, Chung M, Dubra A, Hunter JJ, Merigan WH, Williams DR. Imaging retinal mosaics in the living eye. *Eye*. 2011;25: 301–308.
32. Miller DT, Williams DR, Morris GM, Liang J. Images of cone photoreceptors in the living human eye. *Vision Res*. 1996;36: 1067–1079.
33. Roorda A, Williams DR. The arrangement of the three cone classes in the living human eye. *Nature*. 1999;397:520–522.
34. Carroll J, Neitz M, Hofer H, Neitz J, Williams DR. Functional photoreceptor loss revealed with adaptive optics: an alternate cause of color blindness. *Proc Natl Acad Sci U S A*. 2004;101: 8461–8466.
35. Wolfing JI, Chung M, Carroll J, Roorda A, Williams DR. High-resolution retinal imaging of cone-rod dystrophy. *Ophthalmology*. 2006;113:1019.e1.
36. Carroll J, Choi SS, Williams DR. In vivo imaging of the photoreceptor mosaic of a rod monochromat. *Vision Res*. 2008;48:2564–2568.
37. Vilupuru AS, Rangaswamy NV, Frishman LJ, et al. Adaptive optics scanning laser ophthalmoscopy for in vivo imaging of lamina cribrosa. *J Opt Soc Am A Opt Image Sci Vis*. 2007;24: 1417–1425.
38. Morgan JIW, Dubra A, Wolfe R, Merigan WH, Williams DR. In vivo autofluorescence imaging of the human and macaque retinal pigment epithelial cell mosaic. *Invest Ophthalmol Vis Sci*. 2008;50:1350–1359.
39. Ivers KM, Li C, Patel N, et al. Reproducibility of measuring lamina cribrosa pore geometry in human and nonhuman primates with in vivo adaptive optics imaging. *Invest Ophthalmol Vis Sci*. 2011;52:5473–5480.
40. Zhong Z, Song H, Chui TY, et al. Noninvasive measurements and analysis of blood velocity profiles in human retinal vessels. *Invest Ophthalmol Vis Sci*. 2011;52:4151–4157.
41. Akagi T, Hangai M, Takayama K, et al. In vivo imaging of lamina cribrosa pores by adaptive optics scanning laser ophthalmoscopy. *Invest Ophthalmol Vis Sci*. 2012;53:4111–4119.
42. Chui TY, Vannasdale DA, Burns AB. The use of forward scatter to improve retinal vascular imaging with an adaptive optics scanning laser ophthalmoscope. *Biomed Opt Express*. 2012;3: 2537–2549.
43. Zhong Z, Huang G, Chui TY, et al. Local flicker stimulation evokes local retinal blood velocity changes. *J Vis*. 2012;12(6): 3.
44. Chui TY, Gast TJ, Burns SA. Imaging of vascular wall fine structure in human retina adaptive optics scanning laser ophthalmoscopy. *Invest Ophthalmol Vis Sci*. 2013;54:7115–7124.
45. Pinhas A, Dubow M, Shah N, et al. In vivo imaging of human retinal microvasculature using adaptive optics scanning light ophthalmoscope fluorescein angiography. *Biomed Opt Express*. 2013;4:1305–1317.
46. Sredar N, Ivers KM, Queener HM, et al. 3D modeling to characterize lamina cribrosa surface and pore geometries using in vivo images from normal and glaucomatous eyes. *Biomed Opt Express*. 2013;4:1153–1165.
47. Burns SA, Elsner AE, Chui TY, et al. In vivo adaptive optics microvascular imaging in diabetic patients without clinically


Investigative Ophthalmology & Visual Science

severe diabetic retinopathy. *Biomed Opt Express*. 2014;5:961–974.

48. Kocaoglu OP, Cense B, Jonnal RS, et al. Imaging retinal nerve fiber bundles using optical coherence tomography with adaptive optics. *Vision Res*. 2011;51:1835–1844.
49. Takayama K, Ooto S, Hangai M, et al. High-resolution imaging of the retinal nerve fiber layer in normal eyes using adaptive optics scanning laser ophthalmoscopy. *PLoS One*. 2012;7: e33158.
50. Takayama K, Ooto S, Hangai M, et al. High-resolution imaging of retinal nerve fiber bundles in glaucoma using adaptive optics scanning laser ophthalmoscopy. *Am J Ophthalmol*. 2013;155:870–881.
51. Scoles D, Higgins BP, Cooper RF, et al. Microscopic inner retinal hyper-reflective phenotypes in retinal and neurologic disease. *Invest Ophthalmol Vis Sci*. 2014;55:4015–4029.
52. Huang G, Gast TJ, Burns SA. In vivo adaptive optics imaging of the temporal raphe and its relationship to the optic disc and fovea in the human retina. *Invest Ophthalmol Vis Sci*. 2014; 55:5952–5961.
53. Yang Q, Reisman CA, Wang Z, et al. Automated layer segmentation of macular OCT images using dual-scale gradient information. *Opt Express*. 2010;18:21283–21307.
54. Raza AS, Cho JS, de Moraes CGV, et al. Retinal ganglion cell layer thickness and local visual field sensitivity in glaucoma. *Arch Ophthalmol*. 2011;129:1529–1536.
55. Dubra A, Sulai Y. Reflective afocal broadband adaptive optics scanning ophthalmoscope. *Biomed Opt Express*. 2011;2: 1757–1768.
56. Dubra A, Harvey Z. Registration of 2D images from fast scanning ophthalmic instruments. In: Fischer B, Dawant B, Lorenz C, eds. *The 4th International Workshop on Biomedical Image Registration*. Lubeck, Germany: Springer Berlin Heidelberg; 2010:60–71.
57. Smith G, Atchison DA. *The Eye and Visual Optical Instruments*. 1st ed. Cambridge, UK: Cambridge University Press; 1997.
58. Su D, Park SC, Simonson JL, Liebmann JM, Ritch R. Progression patterns of initial parafoveal scotomas in glaucoma. *Ophthalmol*. 2013;120:520–527.

Investigative Ophthalmology & Visual Science